

Orbital and Spin-Orbit Torque Interplay in Ta/W-based Magnetic Tunnel Junctions with Vertical Non-local Switching

Marco Biagi,^{*,†} Corrado C. M. Capriata,[†] Corentin Bouchard,[†] Subham Kintali
Senapati,[‡] Ioannis Trikoilis Koll,[‡] Ricardo C. Sousa,[‡] Louis Hutin,[†] Bernard
Viala,[†] and Kevin Garello^{*,‡}

[†]*CEA-Leti Minatec, Grenoble, France*

[‡]*Univ. Grenoble Alpes, CEA, CNRS, Grenoble-INP, SPINTEC*

E-mail: marcobiagi97@gmail.com; kevin.garello@cea.fr

Abstract

Spin-orbit torque (SOT) enables ultra-fast, energy-efficient magnetization switching, making it a promising mechanism for introducing MRAMs for cache memory applications. However, current SOT-MRAM devices face write efficiency limitations, with charge-to-spin conversion (ξ_{DL}) reaching $\sim 45\%$, far below the projected $\sim 80\%$ needed to comply with the current delivery of advanced transistor nodes. Recent advances in orbital current physics, evidenced in a wide class of materials, offer a path to enhance ξ_{DL} . Here, we study the Ta(3–30 nm)/W(1–4 nm) system, revealing a large additional spin-orbit torque contribution arising from Ta, a four-fold increase compared to the spin Hall effect in Ta alone, attributed to the orbital Hall contribution. This system exhibits larger ξ_{DL} than W-based SOT systems with more robust perpendicular magnetic anisotropy and compatibility with 400°C annealing. Leveraging

these advantages, we integrate the Ta/W system into 3-terminal SOT-MTJ devices, showing a level of performance similar to that of W-based systems. Our results show that orbital physics can be easily integrated into SOT-MTJ systems, offering a viable strategy to enhance SOT-MRAM efficiency. In addition, we propose and demonstrate a proof-of-concept for vertical non-local switching of SOT-MTJ using orbital torques, simplifying bottom-pinned SOT-MRAM fabrication.

Introduction

The development of electrically controlled nanomagnets for spintronics applications is attracting significant attention, particularly for the realization of non-volatile magnetic memories (MRAMs).¹ This interest is driven by the pressing challenges faced by the microelectronics industry due to the volatility of CMOS-based cache memory elements, such as SRAM and eDRAM.² Spin-transfer-torque (STT)-MRAM is a low-power, high-speed non-volatile memory technology that has already been commercialized as embedded MRAM (eMRAM) and is currently under development for implementation in last-level cache memories. Spin-orbit torque (SOT)-based magnetic tunnel junctions (MTJs) are considered a next-generation MRAM technology, targeting the replacement of SRAM owing to their fast switching processes and high endurance.¹ In such a structure (Fig. 1a), the spin current controlling the switching is generated by a non-magnetic material, typically a heavy metal (HM), due to the spin Hall effect (SHE) and the Rashba-Edelstein effect (REE).³⁻⁵

While some important roadblocks have been overcome, such as the realization of deterministic switching without a magnetic field,⁶⁻⁸ scaling,⁹ and array-level demonstration,¹⁰ the technology requirements are still not met: the write current has to be less than 150 μA , and the currently available SOT materials show moderate efficiencies, high resistivity, and are limited to relatively low thicknesses. Although giant SOT efficiency materials like topological insulators have already been demonstrated to improve SOT switching efficiency,¹¹ their use is still currently hindered by industrial integration process requirements, such as total

thermal budget and non-degrading MTJ specifications.

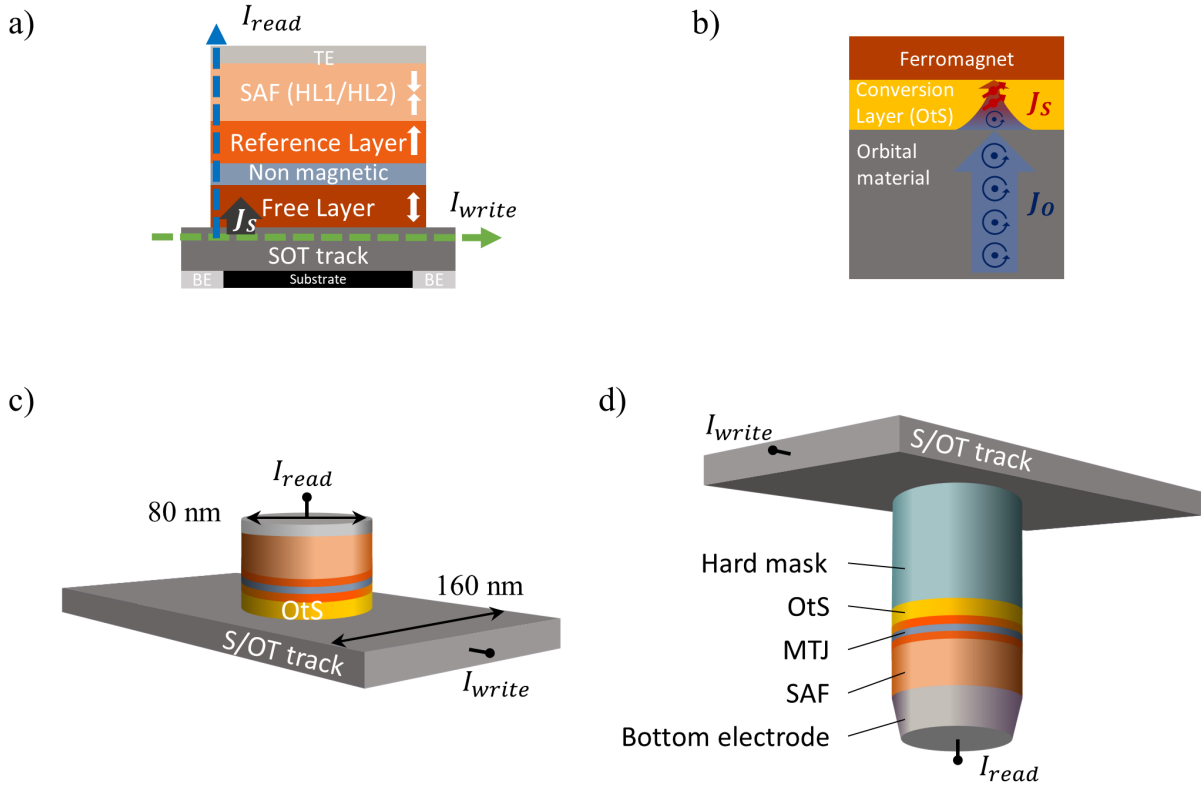


Figure 1: a) Sketch of a 3-terminal SOT-MTJ. The write current is injected in the SOT track, generating a spin current J_s that is transferred to the free layer, while the state of the MTJ is read via TMR. b) Orbital to spin conversion scheme. The orbital current is generated within the orbital material and subsequently converted into a spin current via the orbital-to-spin conversion layer, before propagating into the ferromagnet. c) Schematic view of the devices measured in this work with S/OT track and pillar dimensions. To be noted that in the case of the reference sample the OtS layer is not present. d) Scheme of the proposed bottom-pinned MTJ. The hard mask is used to propagate the orbital and/or spin current into the free layer of the MTJ, simplifying the fabrication process.

Meanwhile, recent predictions and demonstrations^{12–20} of orbital effects, such as the orbital Hall effect (OHE) and the orbital Rashba-Edelstein effect (OREE), could offer a promising route to improve SOT-MTJ write efficiency. Indeed, they exhibit larger magnitudes and diffusion lengths^{12,21} compared to their spin counterparts, and they are present in a much wider class of materials, including light metals and elements with low resistivity. In an analogous way to SHE and REE, these orbital effects give rise to an orbital current that can propagate into adjacent materials. However, the orbital moment does not directly interact

with the spin moment. Hence, to exploit these effects in SOT-MTJ devices, spin-orbit coupling (SOC) is required to convert the orbital current into spin current. This can be achieved by selecting a ferromagnet (FM) with sizable SOC, such as Ni. Another solution, which has the benefit of a less restrictive material choice, is to introduce a strong SOC conversion layer between the orbital source and the ferromagnet (Fig. 1b).^{17–19,22} In this configuration, the orbital current is converted by the Orbital-to-Spin (OtS) conversion layer and transferred to the ferromagnet. Moreover, if the spacer is a heavy metal, two independent channels of spin current are expected to add up linearly to the total effective spin Hall conductivity, possibly increasing the total effective efficiency of the system $\xi_{DL} = (\xi_{DL}^{HM} + \eta_{LS}^{HM} \theta_{OH}^{OS})$, where ξ_{DL}^{HM} is the damping-like efficiency of the HM, η_{LS}^{HM} is the OtS conversion efficiency of the HM, θ_{OH}^{OS} is the orbital Hall angle of the orbital source material.¹⁷

Although still debated,²³ several recent experimental studies have reported additional interactions attributed to orbital current effects, observed using different measurement techniques.^{17–19,21,22,24–27} Experiments have shown how SOC can mediate the transfer of angular momentum to local moments, inducing dynamics of the magnetization and corroborating the role of orbital currents in current-induced torques^{16,28} and their inter-conversion to/from spin currents.^{17,19,22,27}

In this study, we identify a technologically relevant OtS conversion material system, Ta/W, that shows perpendicular magnetic anisotropy (PMA), is back-end-of-line (BEOL) compatible (400 C annealing), and has high efficiency. Ta has the advantage of being compatible with industrial fabrication processes and of exhibiting a large orbital Hall angle θ_{OH} .^{16,20} W has large SOC and a large ξ_{DL} ,²⁹ resulting in an efficient conversion of the orbital current from Ta. In addition, W and Ta can generate a secondary channel of spin current via SHE, further increasing the total effective current-to-spin conversion efficiency. We systematically quantified the effective damping-like efficiency ξ_{DL} as a function of both the conversion layer thickness and the orbital layer thickness on annealed Hall bar samples. In a second step, we fabricated 3-terminal SOT-MTJ devices with 80 nm pillar diameter

devices, and we benchmarked the switching performance of the Ta/W material system (Fig. 1c) against our standard W-based SOT-MTJ. Our results demonstrate not only the successful integration of the OtS conversion scheme in an industrially compatible system but also an enhancement in switching performance. Finally, we extend this work to a proof-of-concept demonstration of vertical non-local switching in SOT-MTJ mediated by orbital torques and discuss its implications for the development of bottom-pinned SOT-MRAM (Fig. 1d).

Results and discussion

Material study

With the conversion scheme depicted in Fig. 1b, it is not possible to directly disentangle the spin and orbital contributions to the total effective ξ_{DL} . Hence, we first systematically quantify, via harmonic Hall voltage method (HHV),³⁰ the ξ_{DL} of the reference stack with only the heavy metal (HM) SOT layer sub//W(t)/FeCoB(1)/MgO(1.25)/FeCoB(0.5)/Ta(3), and sub//Ta(t)/FeCoB(1)/MgO(1.25)/FeCoB(0.5)/Ta(3) (numbers are layer thicknesses in nm) as a function of the HM layer thickness $t_{W,Ta}$, and we compare it to the ξ_{DL} quantified in the orbital stacks sub//Ta(t)/W(1.5)/FeCoB(1)/MgO(1.25)/FeCoB(0.5)/Ta(3), and sub//Ta(20)/W(t)/FeCoB(1)/MgO(1.25)/FeCoB(0.5)/Ta(3) as a function of t_W or t_{Ta} . All samples were annealed at 300°C for 10 minutes in a rapid thermal annealing stage under vacuum. The OtS samples (Ta/W) were additionally annealed at 400°C, a requirement to fulfill BEOL process requirements, as well as revealing its impact on M_S , B_k , and ξ_{DL} .

The measurement geometry for the HHV method is illustrated in Fig. 2a). A 10 Hz a.c. current is applied along the Hall bar channel, and the sample can be rotated in a variable external magnetic field B_{ext} . All measurements are performed at a constant current density $J_{in} = 2 \text{ MA/cm}^2$, calculated by considering the total thickness of the conductive layers (i.e., also considering the FeCoB(1)). From the first and second harmonic resistance, one can quantify the effective damping-like SOT efficiency ξ_{DL} and the effective field-like efficiency

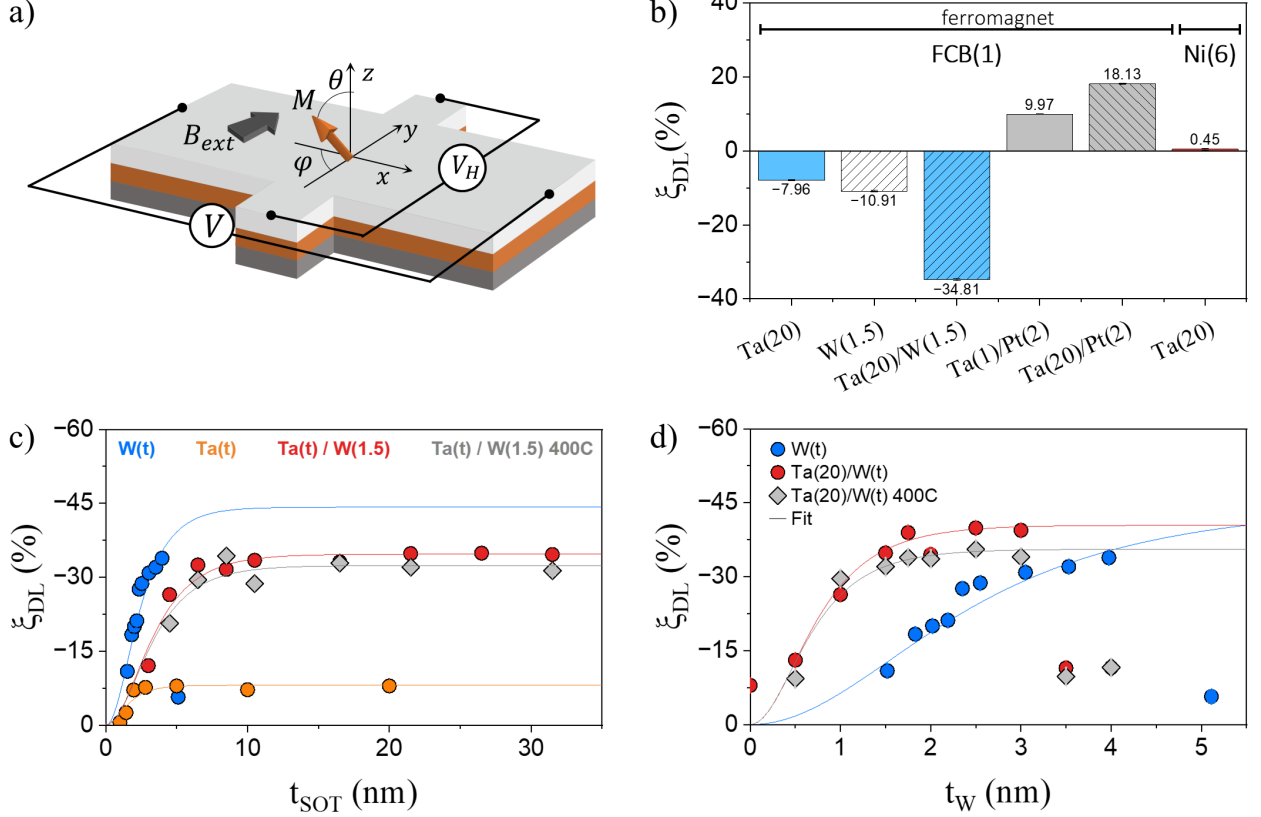


Figure 2: a) Harmonic Hall voltage measurement scheme. An a.c. current $I_{a.c.}$ is injected in the Hall bar, and the Hall voltage is measured as a function of the angle φ of the external in-plane field B_{ext} . b) Damping-like efficiency (ξ_{DL}) for different stack compositions: Ta(20), W(1.5), Ta(20)/W(1.5), Pt(2), Ta(20)/Pt(2), and Ta(20)/Ni(6) (ferromagnet is FeCoB(1) if not specified otherwise). Ta and W show negative spin Hall conductivity while it is positive for Pt. Notably, when the ferromagnet is changed from FeCoB to Ni for the Ta sample, also σ_{SH} changes sign, indicating the presence of an additional contribution that can be attributed to orbital physics. c) ξ_{DL} dependence on the S/OT material thickness for W(t_W), Ta(t_{Ta}), and Ta(t_{Ta})/W(1.5) after $300^\circ C$ annealing. The Ta/W efficiency is also shown for the annealed samples at $400^\circ C$. d) ξ_{DL} dependence on the SOT material thickness for W(t_W), and Ta(20)/W(t_W) after $300^\circ C$ annealing (also $400^\circ C$ for Ta/W). Numbers in parentheses are layer thickness in nm.

ξ_{FL} . $\xi_{DL,FL}$ are defined by normalizing $B_{DL,FL}$ by the injected current density J_{in} :

$$\xi_{DL,FL} = \frac{2e}{\hbar} \frac{M_S t_{FM}}{J_{in}} B_{DL,FL} \quad (1)$$

Where $B_{DL,FL}$ are the experimentally measured damping-like and field-like effective fields. The ξ_{FL} are reported in the supplementary information. The ξ_{DL} of the reference samples W, Ta, and the Ta/W OtS system is summarized as a function of the SOT track thickness

($t_{SOT} = t_W, t_{Ta}, t_{Ta+W(1.5)}$) in Fig. 2c. The data are fitted with the drift-diffusion equation (solid lines) $\xi_{DL}(t_{SOT}) = \xi_{sat}[1 - \text{sech}(t_{SOT}/\lambda)]^{5,19,31}$ to estimate the spin diffusion length λ and the saturation value ξ_{sat} , resulting in $\lambda_W = 1.75$ nm, $\lambda_{Ta} = 1.14$ nm, $\lambda_{Ta(t)/W} = 2.45$ nm, $\xi_{sat}^W = -44.2\%$, $\xi_{sat}^{Ta} = -9.9\%$, and $\xi_{sat}^{Ta(t)/W} = -34.7\%$. It is worth noting that these values are obtained under the assumption of transparent interfaces and therefore underestimate the intrinsic value of ξ_{DL} .

Interestingly, ξ_{DL} increases with increasing t_{SOT} in all systems, suggesting that the main current-to-spin conversion mechanism is of bulk origin (i.e., SHE/OHE). However, the Ta(1.5)/W(1.5) sample shows considerably lower resistivity compared to the thicker Ta(t)/W(1.5) samples ($\rho_{Ta(1.5)/W(1.5)} \sim 84 \mu\Omega\text{cm}$ and $\rho_{Ta(t)/W(1.5)} \sim 140 \mu\Omega\text{cm}$), indicating that the W in our samples stabilizes in a mixed α/β phase when grown on a thin Ta underlayer. This is further confirmed by resistivity maps performed on Ta/W wedges, showing that the W transition happens at lower thicknesses when Ta is thinner (supplementary information). Since the ξ_{DL} thickness dependence is influenced by this phase-transition, this adds uncertainty in identifying the role of bulk/interfacial (OHE/OREE) as the origin of the quantified torque.

Nevertheless, we find that the Ta/W(1.5) system attains the same values of ξ_{DL} as the W reference system. These results are surprising if we take into account that we are using only 1.5 nm of W as a conversion layer, which shows a $\xi_{DL} = 10.9\%$. Consequently, if we compare the DL efficiency of the W(1.5), Ta(20), and Ta(20)/W(1.5) samples, the efficiency in the Ta/W system is enhanced by a factor of 3.2 with respect to the W(1.5) sample and by 4.4 with respect to the Ta(20) sample. Importantly, these samples were also annealed at 400°C, and the efficiency values of the orbital stack were found to be only marginally affected, with $\xi_{sat, Ta(t)/W}^{400^\circ\text{C}} = -32.4\%$ and $\lambda_{Ta(t)/W}^{400^\circ\text{C}} = 2.41$ nm. Meanwhile, the anisotropy is significantly enhanced, from $B_k \approx 0.5$ T to $B_k \approx 1.1$ T, which translates to improved thermal retention and PMA at the device level.

The sign of ξ_{DL} is found to be negative, although θ_{OH} is predicted to be positive for

Ta and W. This points to the fact that the orbital current is converted with the sign of the SOC of the conversion material, which is negative for W.^{14–16,19,27} This is confirmed when substituting W with Pt as the conversion layer; we observe an opposite sign of ξ_{DL} corresponding to the sign of SOC in Pt, and we consistently measure an enhancement of ξ_{DL} in Ta(20)/Pt(2) compared to the Pt reference sample (Fig. 2b).

To further identify the presence of orbital effects in Ta, we fabricated a Ta(20)/Ni(6) sample. Ni is known for its relatively large positive SOC, which should allow for the conversion of orbital current without requiring an OtS layer.^{13,16,17,20,32} In this scenario, the measured efficiency should reflect the interplay between the negative spin Hall effect (SHE) in Ta and the positive OtS conversion in Ni. The fact that our measurements show a small but positive ξ_{DL} suggests that, within the two-channel current model picture, orbital effects in Ta are significant and that the OtS conversion by Ni of orbital current in Ta dominates over the SHE generated in Ta.

Then, we investigated the dependence of ξ_{DL} on W thickness in Ta(20)/W(*t*) samples, as shown in Fig. 2d. The efficiency is consistently enhanced with respect to the reference samples. In particular, we observe a maximum value of ξ_{DL} ($\xi_{DL} = -39.90\%$ for $t_W = 2.5$ nm) in the Ta/W system, which is 18% larger than the highest value of ξ_{DL} in the reference samples ($\xi_{DL} = -33.87\%$ for $t_W = 4$ nm). This can be interpreted as the constructive combination of the SHE generated by W and OHE/OREE generated by Ta. Meanwhile, the shallow decrease of $\xi_{DL}^{Ta/W}$ at about $t_W = 1.75$ nm can be understood by considering that when the thickness of the conversion layer exceeds the spin diffusion length in W, scattering events with spin-flips become dominant, and the spin-orbital conductivity saturates to a finite value determined by the SHE in the conversion layer.¹⁹ However, it is difficult to draw clear conclusions as there is a sharp drop at $t_W = 3$ nm, which is due to the β -to- α transition phase of W, known to occur around 4 nm for annealed W on SiO_x, and to lower thicknesses when W is grown on a thin metallic seed.^{33,34} In the case of 400°C annealing, we report similar trends to the 300°C case, but with a slight reduction in efficiency values of about 13% in

1 nm < t_W < 3 nm, and a more pronounced plateau.

Finally, we tentatively separate the contributions from the SHE and OHE in the orbital stacks by means of a simple current distribution model in the saturation region for the Ta(20)/W(1.5) sample. We first estimate the resistivity of W and Ta by linearly fitting the conductance over the variation of the layer thickness in W(t), Ta(t), Ta(t)/W, and Ta/Pt(t) sample series, $G_{tot} = \frac{\sigma_X w}{l} t_X + G_{rest}$, where X = W, Ta, Pt, G_{rest} is the conductance of the fixed thickness layers in the samples, w is the Hall bar width, and l is the distance between the Hall bar arms used to monitor sample resistivity. Using the quantified efficiencies of W(1.5)/FeCoB and Ta(20)/FeCoB in the reference samples, one can simply estimate the effective SOT field $B_{DL} = \theta_{DL} \hbar J_c^{layer} / (2eM_{stFM})$ generated by each layer in Ta(20)/W(1.5)/FeCoB(1) by SHE. By subtracting the sum of the two from the experimentally measured SOT field, we estimated the additional contribution supposedly generated by the OtS conversion in Ta(20)/W(1.5), as reported in Table 1.

Table 1: Estimated $\rho_{R_{//}}$ from conductance fit, estimated intrinsic spin Hall angle θ_{DL}^{intr} for reference samples, and B_{DL} contribution separation for OtS samples by means of a simple parallel resistor model.

Stack	Layer	$\rho_{R_{//}}$ [$\mu\Omega\text{cm}$]	I_{stack} [mA]	$J_{R_{//}}^{layer}$	θ_{DL}^{intr} [%]	B_{DL}^{est} [mT]	B_{DL}^{exp} [mT]	B_{DL}^{OT} [mT]
W(1.5)/FeCoB(1)	W(1.5)	138.9 ± 6.3	0.50	1.51	-14.45			
Ta(20)/FeCoB(1)	Ta(20)	145.7 ± 2.6	4.20	1.94	-8.20			
Ta(1)/Pt(2)/FeCoB(1)	Pt(2)	67.5 ± 17.3	0.80	2.93	6.93			
Ta(20)/W(1.5)/FeCoB(1)	W(1.5)		4.50	2.01		-0.87	-2.30	-1.20 ± 0.24
	Ta(20)			1.92		-0.47		
Ta(20)/Pt(2)/FeCoB(1)	Pt(2)		4.60	3.87		0.57	0.77	0.36 ± 0.16
	Ta(20)			1.79		-0.31		

In the Ta(20)/W(1.5) sample, we estimate the damping-like effective fields as $B_{DL}^W = -0.87$ mT and $B_{DL}^{Ta} = -0.47$ mT. Even assuming complete transmission of the Ta-generated spin current through the W layer to the ferromagnet, the combined Ta and W contributions are insufficient to account for the measured SOT effective field $B_{DL}^{exp} = -2.30$ mT. This

discrepancy implies an additional contribution of $B_{DL}^{OT} = -1.20 \pm 0.24$ mT, where the uncertainty boundaries correspond to the cases in which the spin current from Ta is either fully transmitted to the FeCoB or completely absorbed by the W layer. Therefore, such a large enhancement cannot be attributed solely to the SHE; rather, it could be explained by orbital current generation in Ta and its subsequent conversion into spin current in W.

Finally, we estimated the individual layers SHE contribution in Ta(20)/Pt(2)/FeCoB(1). Here, we used a series of Ta(1)/Pt(t)/FeCoB(1) as reference samples, where the layer Ta(1) serves as a seed for better growth of Pt; noting that Ta(1) showed negligible SOT efficiency. In this case, we also find an additional positive contribution of $B_{DL}^{OT} = 0.36 \pm 0.16$ mT, consistent with the OtS conversion scenario.

It is important to note that this model neglects interfacial spin transparency as well as interfacial phenomena such as spin memory loss and spin backflow.³⁵⁻³⁷ When W is grown on Ta, the resulting W(1.5)/FeCoB interface may differ from that obtained when W is deposited on SiO₂, potentially leading to enhanced spin transmission in the Ta/W system due to better interfacial quality. However, we observe that: (i) the enhancement in damping-like efficiency is observed in both the Ta/W system and the Ta/Pt system; (ii) the sign of ξ_{DL} is consistent with the sign of the spin Hall angle of the conversion layer; (iii) in the Ta/Ni system, a positive DL efficiency is observed, in agreement with the sign of the SOC of Ni. These results point more strongly to an orbital-to-spin conversion scenario.

For the field-like torque (supplementary information), surprisingly, we do not observe a reduction as expected when W turns into alpha, suggesting the presence of a non-negligible spin accumulation at the W/FCB interface that is independent of W.

Device switching characterization

Building on blanket sample findings, we fabricated three-terminal MTJs that include W as a reference material and an OtS stack to assess its switching performance at the device level (Fig.1c). The OtS sample consists of Sub//Ta(10)/W(1.5)/FeCoB(1)/MgO(1.25)/

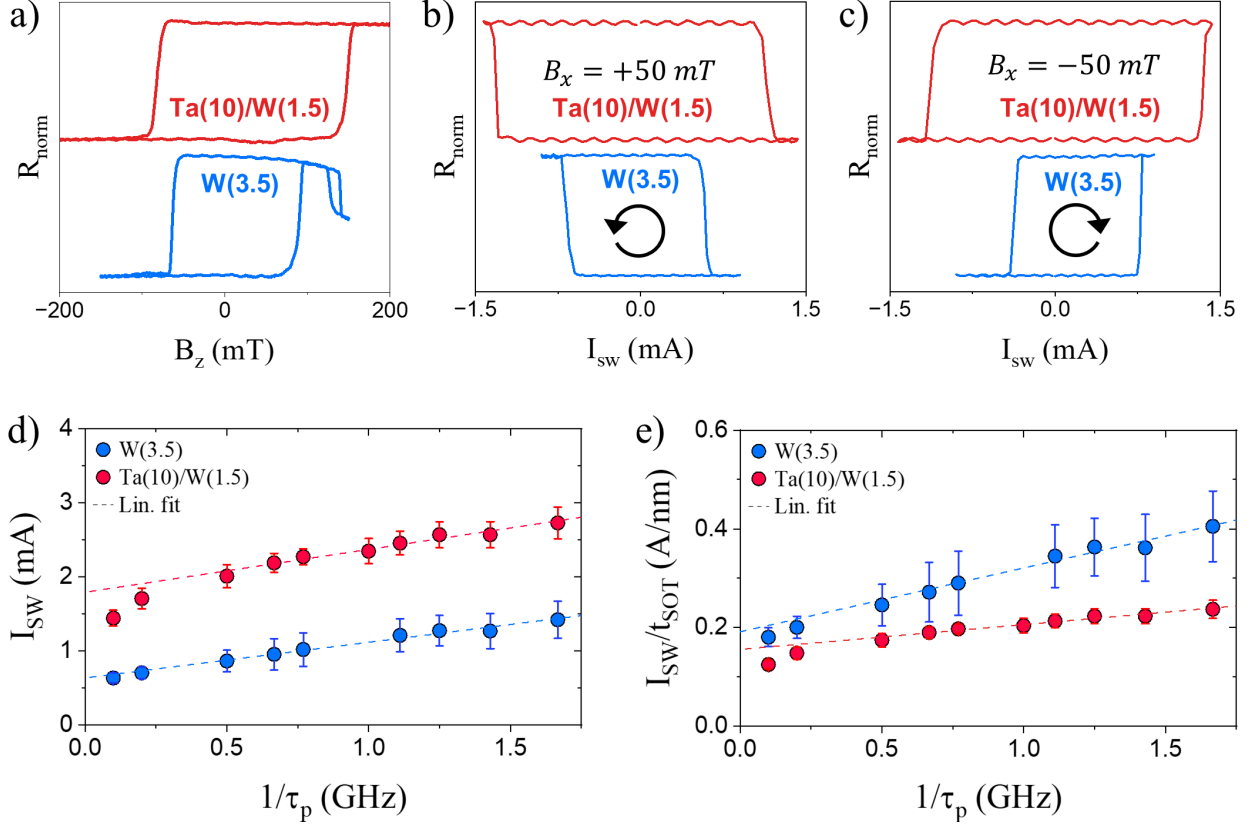


Figure 3: a) 3-terminal SOT-MTJ devices R-H loop, for reference sample W(3.5)/FeCoB(1) and OtS sample Ta(10)/W(1.5). b) Device switching plot for $\tau_P = 10$ ns and $B_x = \pm 50$ mT, for reference sample W(3.5)/FeCoB(1) and OtS sample Ta(10)/W(1.5)/FeCoB(1). Also OtS sample shows SOT switching symmetry. c) Switching current I_{SW} dependence on the inverse of the applied pulse length τ_p , for reference and OtS samples. The data are fitted in the intrinsic regime by means of a linear model (see text). d) Normalized I_{SW} on the SOT track thickness below the MTJ t_{SOT} as a function of the inverse of the applied pulse length. Notably, the Ta(10)/W(1.5) samples shows lower switching current values.

FeCoB(1)/SAF, while the reference sample composition is sub//W(3.5)/FeCoB(1)/MgO(1.25)/FeCoB(1)/SAF. In the reference sample, we tuned the etching conditions to stop the pillar etch at the SOT line. In the OtS sample, one of the main advantages is the larger tolerance to the etching margins; therefore, we tuned the etching conditions to leave Ta(7) as the SOT track. The TMR is found to be between 10% and 20% for both W and Ta/W samples. Although weak, it relates more to our MgO stack quality and our fabrication process than to the limitations of these material systems.

Fig. 3a shows that OtS samples have a significantly improved free layer coercive field

$B_c = 116.4$ mT, almost twice as large as that of the W samples. Then, in Fig. 3b,c, we present exemplary switching loops for $\tau_p = 10$ ns and $B_x = \pm 50$ mT. Both samples switch with a clear SOT character, i.e., the polarity depends on the combination of the current and the applied in-plane field polarities. Finally, we characterized the switching current as a function of the applied pulse length down to 500 ps, and we report in Fig. 3d the median switching current I_{SW} averaged over five devices (obtained from 100 loops per device) as a function of the inverse of the pulse length $1/\tau_p$. One can estimate from this measurement the critical current in the intrinsic switching regime, following the model $I_c = I_{c0} + q/\tau_p$, where I_{c0} is the intrinsic critical switching current, and q is an effective charge parameter that determines the rate at which the angular momentum is transferred to the free layer (FL).³⁸ By fitting the data for $\tau_p < 1$ ns, we find $I_{c0}^{W(3.5)} = 0.67$ mA and $I_{c0}^{Ta(10)/W(3.5)} = 1.86$ mA, respectively. However, it should be noted that the Ta/W sample exhibits substantially higher coercivity ($B_C^{W(3.5)} = 63.17$ mT, and $B_C^{Ta(10)/W(1.5)} = 116.4$ mT) and anisotropy ($B_k^{W(3.5)} = 163.8$ mT, and $B_k^{Ta(10)/W(1.5)} = 232.0$ mT), which implies that a lower switching current density is intrinsically required for the W samples. However, the SOT track below the MTJ is nearly four times thicker for the Ta/W sample, which inherently leads to higher absolute switching currents. Hence, to compare the current-to-spin conversion efficiency of the two systems, we normalize I_{SW} by the coercivity of the samples and the SOT track thickness below the MTJ (Fig. 3e). In this case, both systems exhibit comparable values for I_{c0}/B_C , of $I_{c0}^{W(3.5)}/B_C^{W(3.5)} = 0.011$ mA/mT and $I_{c0}^{Ta(10)/W(1.5)}/B_C^{Ta(10)/W(1.5)} = 0.016$ mA/mT. Furthermore, after normalization by the thickness of the SOT track below the pillar, the Ta/W sample achieves a lower I_{c0} than W, particularly $I_{c0}^W/t_W = 0.19$ mA/nm and $I_{c0}^{Ta/W}/t_{Ta/W} = 0.16$ mA/nm. While the two systems show similar switching performances, the Ta/W system provides superior scalability and improved process compatibility in terms of thermal budget (annealing) and tolerance to pillar etching, easing integration and development on a large scale and industrial platforms.

Towards bottom-pinned SOT-MTJ

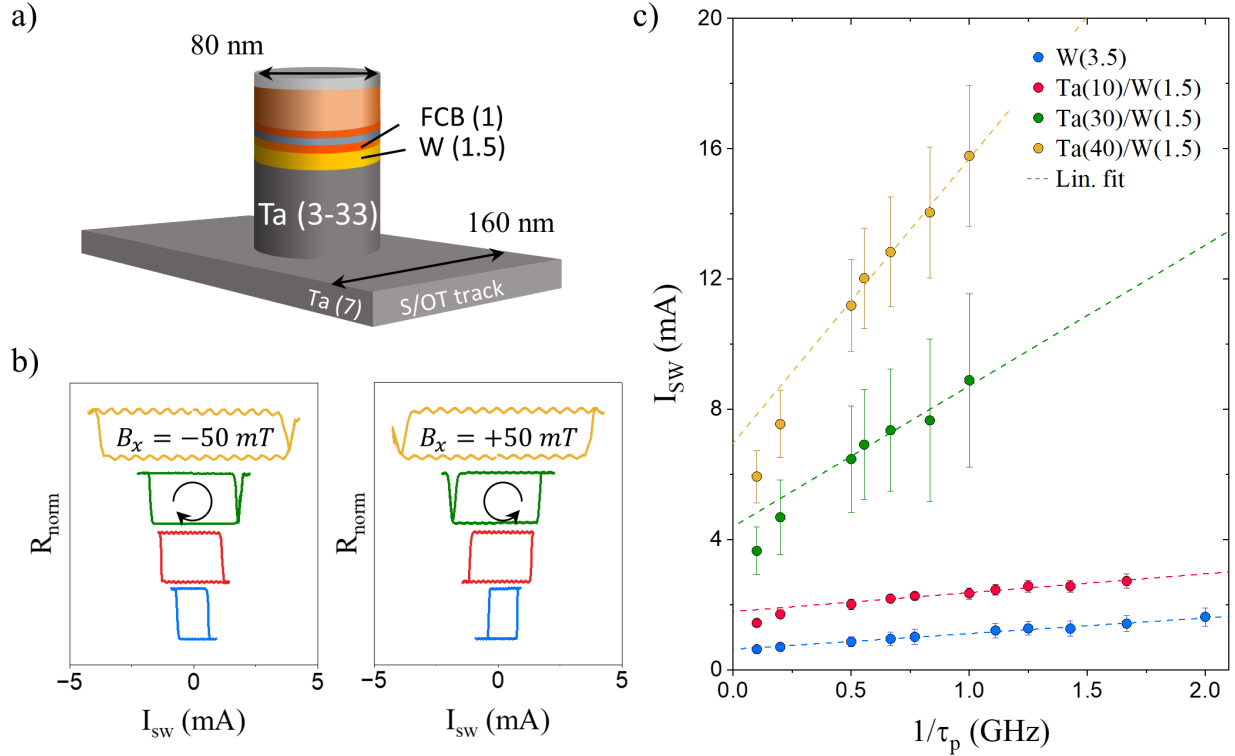


Figure 4: a) Device scheme. The etch is stopped inside the SOT track such as to leave a thick Ta spacer layer between the S/OT track where the current is injected and the OtS/free layer. b) Device switching plots for $\tau_P = 10$ ns and $B_X = \pm 50$ mT, for samples W(3.5), Ta(10)/W(1.5), Ta(30)/W(1.5), and Ta(40)/W(1.5). All samples switch with SOT symmetry. c) I_{SW} dependence on the inverse of the applied pulse length τ_p . The data are fitted in the intrinsic regime by means of a linear model (see text). Notably, switching is observed for all samples. As expected, Ta(30)/W(1.5), and Ta(40)/W(1.5) samples require higher current to switch due to the higher thickness. This is attributed to both the decay of orbital currents in the Ta spacer, and the reduced current in the W layer.

Finally, we leverage our findings to introduce a novel concept of vertical non-local switching in SOT-MTJ devices, which enables a new approach that could greatly simplify the fabrication process of “bottom-pinned” SOT-MTJs. The bottom-pinned design is classically used in commercialized STT-MRAM technology. It consists of designing the stack by placing the FL on top and the SAF at the bottom, which is known to improve MTJ properties by reducing stress on the FL/MgO while additionally improving the yield of the device.^{1,39}

Although the bottom-pinned SOT-MTJ was recently demonstrated,^{40,41} its fabrication requires introducing several critical steps, such as precisely removing the MTJ hard mask without affecting FL properties and depositing sufficiently conformal SOT material. This would hinder its implementation into industrial processes and limit its scaling.

We propose an alternative approach inspired by lateral spin valve (LSV) devices,^{42,43} which is a spin current metrology method in which the spin current injector and detector are spaced hundreds of nanometers apart. It was also demonstrated that it is possible to exploit the non-local (NL) spin current drift to switch magnetic nano-pillars⁴⁴ and 3-terminal STT devices.⁴⁵ We transposed this in-plane NL switching concept to vertical 3-terminal SOT-MTJ devices to introduce a simplified integration scheme (Fig. 1d) of the “bottom-pinned” MTJ.⁴⁶ In analogy with LSV, the spacer layer is the metallic hard mask used to etch the MTJ pillar, the detector is the MTJ free layer, and the spin/orbital current generator is the S/OT line. This design simplifies the fabrication process, introducing minimal changes to the current STT process flow while preserving the benefits of both the bottom-pinned MTJ and the 3-terminal MTJ configuration. Moreover, it has the advantage of being less restrictive on material choice and offers the possibility to exploit novel physics, such as orbital current. Given the limitations of our cleanroom for integrating 3-terminal bottom pinned MTJ, we fabricated additional Ta(30)/W(1.5) and Ta(40)/W(1.5) MTJ samples in a top-pinned configuration to explore the feasibility of the non-local control of S/OT-MTJ (Fig. 4a). 80 nm diameter MTJ pillars were etched down to Ta = 7 nm, separating the S/OT layer and the free layer by 23 (33) nm Ta spacers. Fig. 4b clearly shows SOT symmetry switching in both sample sets.

We report in figure 4c the median switching current I_{SW} averaged over five devices (obtained from 100 loops per device) as a function of the inverse of the pulse length $1/\tau_p$. Notably, we observe switching of the free layer down to 1 ns pulse duration, after which we are limited by the maximum applicable voltage in our experimental setup. The critical switching current I_{c0} increases with the thickness of the patterned Ta pillar. This is expected

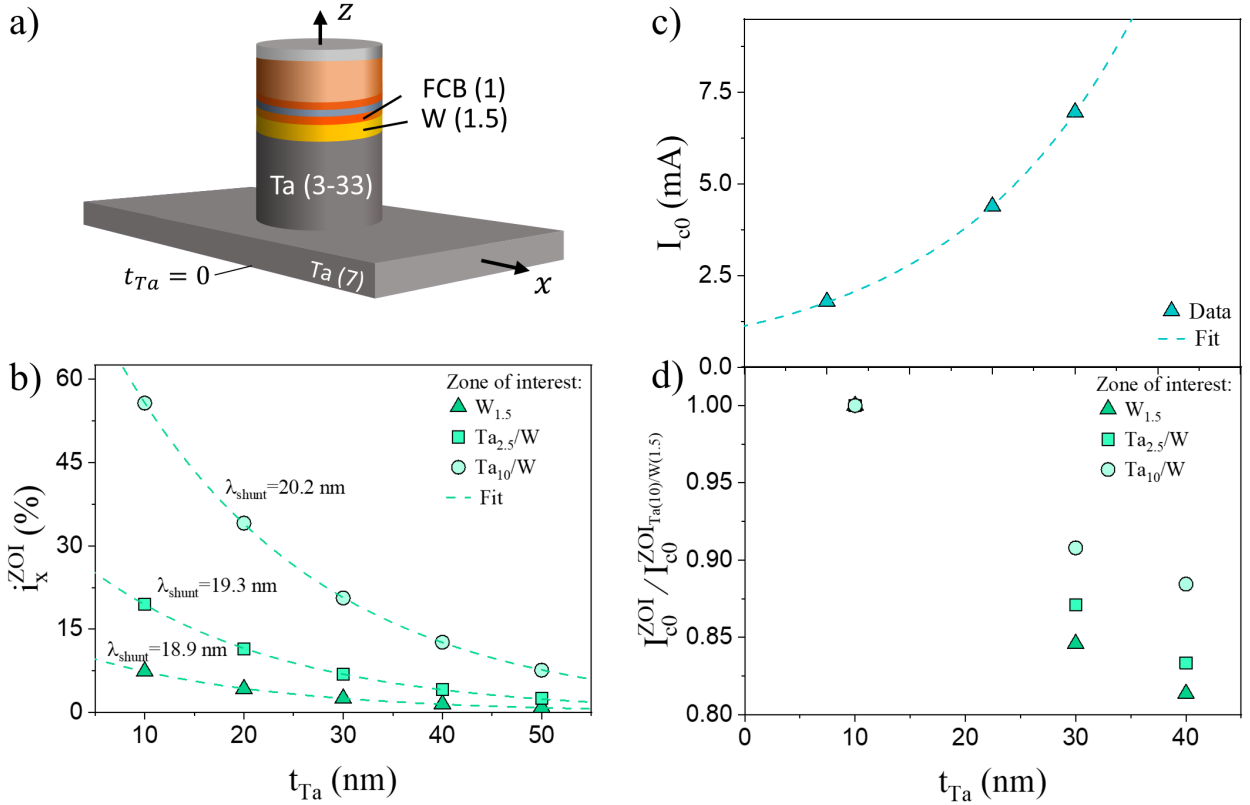


Figure 5: a) Illustration of the simulated and measured MTJ devices. b) Simulated current x -component percentage flowing in $W(1.5)$, $Ta(2.5)/W(1.5)$ and $Ta(10)/W(1.5)$ zone of interest (ZOI) for a given current input, as a function of the total Ta thickness t_{Ta} . c) Experimentally measured intrinsic switching current I_{c0} as a function of t_{Ta} . d) Normalized current fraction at the experimental critical switching current flowing in the zones of interest as a function of t_{Ta} . The critical current fraction $I_{c0}^{ZOI} = i_x^{ZOI} \times I_{c0}$ is normalized by $I_{c0}^{ZOI_{Ta(10)/W(1.5)}} = i_x^{ZOI_{Ta(10)/W(1.5)}} \times I_{c0}^{Ta(10)/W(1.5)}$ that is the fraction of I_{c0} flowing in the ZOI in the $Ta(10)/W(1.5)$ sample. The dotted lines in b) and c) are the exponential fit from which we extract the characteristic lengthscale of the shunting effect and the lengthscale over which I_{c0} increases in the measured devices.

to be due to the reduced current flowing in the W and at the Ta/W interface, which decreases the contributions from the SHE of W and the OREE to the total spin current, respectively.

To determine whether the increase in I_{c0} can be explained solely by the shunting effect and associated reduced current in W, or whether an additional long-range bulk contribution (possibly arising from the OHE) is present, we performed COMSOL simulations to estimate the shunting length in the Ta/W system. Here, the shunting length λ_{shunt} is the characteristic electrical length-scale describing the current redistribution and partial leakage in the MTJ pillar due to the shunting effect. We quantified from simulations i_x^{ZOI} , the current percentage

flowing in the zones of interest (ZOI). The ZOI includes the possible “effective volumes” contributing to switching; i.e., the W(1.5) layer alone, the Ta(2.5)/W(1.5), and Ta(10)/W(1.5). To differentiate them from the sample nomenclature, we denote them as $W_{1.5}$, $Ta_{2.5}/W$, and Ta_{10}/W . In the simulations, we used the resistivity values estimated from the conductance fit reported in Tab. 1. The results of the simulations are reported in Fig. 5b. By fitting the decrease of i_x^{ZOI} with a current decay diffusion model $i_x^{ZOI}(t_{Ta}) = Ae^{-t_{Ta}/\lambda_{shunt}}$,^{42,47} we extract a shunting characteristic length-scale of $\lambda_{shunt}^{W_{1.5}} = 18.9$ nm, $\lambda_{shunt}^{Ta_{2.5}/W} = 19.3$ nm, and $\lambda_{shunt}^{Ta_{10}/W} = 20.2$ nm.

We then fit the experimental values of I_{c0} with $I_{c0}(t_{Ta}) = Be^{t_{Ta}/\lambda_{exp}}$ (Fig.5c), where λ_{exp} represents an effective characteristic length-scale of the system to be compared with the simulated value λ_{shunt} . The fit yields $\lambda_{exp} = 22.0$ nm. Although only three data points are available, the exponential dependence provides a reasonable description of the data, indicating that the shunting effect is the dominant factor responsible for the increase in I_{c0} . It is worth noting that the simulation with COMSOL neglects the effects of the interfaces and other non-idealities in our system; therefore, it overestimates the real shunting length. We find $\lambda_{exp} > \lambda_{shunt}$ of 16.4% (14%) when considering $W_{1.5}$ ($Ta_{2.5}/W$) as an effective switching volume. Interestingly, we still find $\lambda_{exp} > \lambda_{shunt}$ of about 9% even if we consider 10 nm of Ta to contribute to the switching.

To further confirm the presence of an additional long-range contribution, we calculated the reduction of the critical switching current in the ZOI in the different Ta thickness samples, calculated as $I_{c0}^{ZOI} = i_x^{ZOI} \times I_{c0}$. Fig 5d shows I_{c0}^{ZOI} normalized by $I_{c0}^{ZOI_{Ta(10)/W(1.5)}}$ (i.e., the current flowing in the ZOI in the Ta(10)/W(1.5) sample) as a function of the total Ta thickness below the ferromagnet. We find that the critical switching current for the three ZOI decreases as the Ta thickness increases. In particular, the critical switching current in the $W_{1.5}$ ($Ta_{2.5}/W$) layer is about 19% (17%) less in Ta(40)/W(1.5) than in Ta(10)/W(1.5) samples. If switching were governed exclusively by the local current flowing into the ZOI, the critical switching current would be expected to be independent of the Ta thickness. Taken

together with the previous observations, these estimates are consistent with the presence of an additional long-range contribution that grows with t_{Ta} .

Conclusions

In conclusion, we systematically investigated the thickness dependence of the SOT efficiency for W, Ta, and Ta/W as a function of both W and Ta thicknesses. We found a $\sim 20\%$ enhancement in efficiency for the Ta/W bilayer compared to the reference W samples, which we attribute to orbital physics. We estimated that this additional contribution is comparable in magnitude to the spin Hall effect from W(1.5) and that it represents $\sim 50\%$ of the total measured B_{SOT} . In addition, the Ta/W-based system exhibits large perpendicular magnetic anisotropy and is compatible with $400^\circ C$ annealing, an important requirement for the MRAM industrial integration process. We successfully transferred this orbital-to-spin conversion scheme into 3-terminal S/OT-MTJ and benchmarked their switching performances against standard W-based devices. While Ta/W systems require more current to switch due to a fourfold increase in thickness, they demonstrate superior switching efficiency compared to W samples when normalized by the thickness below the MTJ, highlighting significant potential for optimization. Finally, we provided indications of long-range orbital diffusion in the MTJ, further supported by the COMSOL current-density distribution simulations. However, the relatively limited orbital diffusion length of the investigated materials remains a key constraint. This suggests a promising pathway toward non-local control of MTJs through orbital transport mechanisms by exploring materials with longer orbital diffusion lengths.

In conclusion, our results underscore that orbital physics can be harnessed to improve SOT writing performance in SOT-MTJ, and that the Ta/W system has the potential to outperform the current standard W-based systems in terms of critical switching current while maintaining fast operation and showing superior MTJ properties, as well as room for SOT track optimization. This achievement opens a promising pathway for a simplified

integration of bottom-pinned SOT-MTJs.

Acknowledgement

This work was supported by the France 2030 government investment plan, managed by the French National Research Agency under grant reference PEPR Electronique (ANR-22-PEEL-0009); by the French RENATECH network, implemented on the Upstream Technological Platform in Grenoble (PTA) (ANR-22-PEEL-0015); by the Carnot project PRIME SPOT (ANR P-22-03813); by the Horizon Europe grant 101183277 in the framework of the Chips JU NanoIC Pilot Line; and by ORCHID program (project 52694UJ), funded by the French Ministry for Europe and Foreign Affairs, and for Higher Education and Research and the National Science and Technology Council. The authors thank Jerome Faure-Vincent and Stephane Auffret for sample deposition and material development, Alain Marty and Gwenael Acheson for technical support, and YoshiChika Otani for valuable scientific discussions.

References

- (1) Krizakova, V.; Perumkunnil, M.; Couet, S.; Gambardella, P.; Garello, K. Spin-orbit torque switching of magnetic tunnel junctions for memory applications. *Journal of Magnetism and Magnetic Materials* **2022**, *562*, 169692.
- (2) Molas, G.; Nowak, E. Advances in Emerging Memory Technologies: From Data Storage to Artificial Intelligence. *Applied Sciences* **2021**, *11*, 11254.
- (3) Dyakonov, M.; Perel, V. Current-induced spin orientation of electrons in semiconductors. *Physics Letters A* **1971**, *35*, 459–460.
- (4) Sinova, J.; Valenzuela, S. O.; Wunderlich, J.; Back, C.; Jungwirth, T. Spin Hall effects. *Reviews of Modern Physics* **2015**, *87*, 1213–1260.

- (5) Manchon, A.; Železný, J.; Miron, I.; Jungwirth, T.; Sinova, J.; Thiaville, A.; Garello, K.; Gambardella, P. Current-induced spin-orbit torques in ferromagnetic and antiferromagnetic systems. *Reviews of Modern Physics* **2019**, *91*.
- (6) Garello, K. et al. SOT-MRAM 300MM Integration for Low Power and Ultrafast Embedded Memories. 2018 IEEE Symposium on VLSI Circuits. 2018.
- (7) Wang, M.; Cai, W.; Zhu, D.; Wang, Z.; Kan, J.; Zhao, Z.; Cao, K.; Wang, Z.; Zhang, Y.; Zhang, T.; Park, C.; Wang, J.-P.; Fert, A.; Zhao, W. Field-free switching of a perpendicular magnetic tunnel junction through the interplay of spin-orbit and spin-transfer torques. *Nature Electronics* **2018**, *1*, 582–588.
- (8) Shao, Q.; Li, P.; Liu, L.; Yang, H.; Fukami, S.; Razavi, A.; Wu, H.; Wang, K.; Freimuth, F.; Mokrousov, Y. Roadmap of spin-orbit torques. *IEEE Transactions on Magnetism* **2021**, *57*, 1–39, Publisher: IEEE.
- (9) Van Beek, S.; Cai, K.; Yasin, F.; Hody, H.; Talmelli, G.; Nguyen, V.; Vergel, N. F.; Palomino, A.; Trovato, A.; Wostyn, K.; Rao, S.; Kar, G.; Couet, S. Scaling the SOT track – A path towards maximizing efficiency in SOT-MRAM. 2023 International Electron Devices Meeting (IEDM). 2023; p 1–4.
- (10) Yasin, F.; Palomino, A.; Kumar, A.; Pica, V.; Van Beek, S.; Talmelli, G.; Nguyen, V.; Cosemans, S.; Crotti, D.; Wostyn, K.; Kar, G. S.; Couet, S. Extremely Scaled Perpendicular SOT-MRAM Array Integration on 300mm Wafer. 2024 IEEE Symposium on VLSI Technology and Circuits (VLSI Technology and Circuits). 2024; pp 1–2.
- (11) Pai, C.-F. Switching by topological insulators. *Nature Materials* **2018**, *17*, 755–757.
- (12) Go, D.; Jo, D.; Kim, C.; Lee, H.-W. Intrinsic Spin and Orbital Hall Effects from Orbital Texture. *Physical Review Letters* **2018**, *121*.

- (13) Go, D.; Freimuth, F.; Hanke, J.-P.; Xue, F.; Gomonay, O.; Lee, K.-J.; Blügel, S.; Haney, P. M.; Lee, H.-W.; Mokrousov, Y. Theory of current-induced angular momentum transfer dynamics in spin-orbit coupled systems. *Physical Review Research* **2020**, *2*.
- (14) Go, D.; Lee, H.-W.; Oppeneer, P. M.; Blügel, S.; Mokrousov, Y. First-principles calculation of orbital Hall effect by Wannier interpolation: Role of orbital dependence of the anomalous position. *Physical Review B* **2024**, *109*.
- (15) Salemi, L.; Oppeneer, P. M. First-principles theory of intrinsic spin and orbital Hall and Nernst effects in metallic monoatomic crystals. *Phys. Rev. Mater.* **2022**, *6*.
- (16) Lee, D. et al. Orbital torque in magnetic bilayers. *Nature Communications* **2021**, *12*.
- (17) Lee, S.; Kang, M.-G.; Go, D.; Kim, D.; Kang, J.-H.; Lee, T.; Lee, G.-H.; Kang, J.; Lee, N. J.; Mokrousov, Y.; Kim, S.; Kim, K.-J.; Lee, K.-J.; Park, B.-G. Efficient conversion of orbital Hall current to spin current for spin-orbit torque switching. *Communications Physics* **2021**, *4*.
- (18) Rothschild, A.; Am-Shalom, N.; Bernstein, N.; Meron, M.; David, T.; Assouline, B.; Frohlich, E.; Xiao, J.; Yan, B.; Capua, A. Generation of spin currents by the orbital Hall effect in Cu and Al and their measurement by a Ferris-wheel ferromagnetic resonance technique at the wafer level. *Physical Review B* **2022**, *106*.
- (19) Sala, G.; Gambardella, P. Giant orbital Hall effect and orbital-to-spin conversion in 3d, 5d, and 4f metallic heterostructures. *Phys. Rev. Res.* **2022**, *4*, 033037.
- (20) Dutta, S.; Tulapurkar, A. A. Observation of nonlocal orbital transport and sign reversal of dampinglike torque in Nb/Ni and Ta/Ni bilayers. *Physical Review B* **2022**, *106*.
- (21) Choi, Y.-G.; Jo, D.; Ko, K.-H.; Go, D.; Kim, K.-H.; Park, H. G.; Kim, C.; Min, B.-C.; Choi, G.-M.; Lee, H.-W. Observation of the orbital Hall effect in a light metal Ti. *Nature* **2023**, *619*, 52–56.

- (22) Gupta, R.; Bouard, C.; Kammerbauer, F.; Ledesma-Martin, J. O.; Bose, A.; Kononenko, I.; Martin, S.; Usé, P.; Jakob, G.; Drouard, M.; Kläui, M. Harnessing orbital Hall effect in spin-orbit torque MRAM. *Nature Communications* **2025**, *16*.
- (23) Valet, T.; Jaffres, H.; Cros, V.; Raimondi, R. Quantum Kinetic Anatomy of Electron Angular Momenta Edge Accumulation. 2025; <https://arxiv.org/abs/2507.06771>.
- (24) Lyalin, I.; Alikhah, S.; Berritta, M.; Oppeneer, P. M.; Kawakami, R. K. Magneto-Optical Detection of the Orbital Hall Effect in Chromium. *Physical Review Letters* **2023**, *131*.
- (25) Kumar, S.; Kumar, S. Ultrafast THz probing of nonlocal orbital current in transverse multilayer metallic heterostructures. *Nature Communications* **2023**, *14*.
- (26) Wang, P.; Feng, Z.; Yang, Y.; Zhang, D.; Liu, Q.; Xu, Z.; Jia, Z.; Wu, Y.; Yu, G.; Xu, X.; Jiang, Y. Inverse orbital Hall effect and orbitronic terahertz emission observed in the materials with weak spin-orbit coupling. *npj Quantum Materials* **2023**, *8*.
- (27) Ding, S.; Ross, A.; Go, D.; Baldrati, L.; Ren, Z.; Freimuth, F.; Becker, S.; Kammerbauer, F.; Yang, J.; Jakob, G.; Mokrousov, Y.; Kläui, M. Harnessing Orbital-to-Spin Conversion of Interfacial Orbital Currents for Efficient Spin-Orbit Torques. *Physical Review Letters* **2020**, *125*.
- (28) Krishnia, S.; Sassi, Y.; Ajejas, F.; Sebe, N.; Reyren, N.; Collin, S.; Denneulin, T.; Kovács, A.; Dunin-Borkowski, R. E.; Fert, A.; George, J.-M.; Cros, V.; Jaffrès, H. Large Interfacial Rashba Interaction Generating Strong Spin–Orbit Torques in Atomically Thin Metallic Heterostructures. *Nano Letters* **2023**, *23*, 6785–6791.
- (29) Pai, C.-F.; Liu, L.; Li, Y.; Tseng, H. W.; Ralph, D. C.; Buhrman, R. A. Spin transfer torque devices utilizing the giant spin Hall effect of tungsten. *Applied Physics Letters* **2012**, *101*, 122404.

- (30) Garello, K.; Miron, I. M.; Avci, C. O.; Freimuth, F.; Mokrousov, Y.; Blügel, S.; Auffret, S.; Boule, O.; Gaudin, G.; Gambardella, P. Symmetry and magnitude of spin-orbit torques in ferromagnetic heterostructures. *Nature Nanotechnology* **2013**, *8*, 587–593.
- (31) Liu, L.; Moriyama, T.; Ralph, D. C.; Buhrman, R. A. Spin-Torque Ferromagnetic Resonance Induced by the Spin Hall Effect. *Physical Review Letters* **2011**, *106*.
- (32) Amin, V. P.; Li, J.; Stiles, M. D.; Haney, P. M. Intrinsic spin currents in ferromagnets. *Physical Review B* **2019**, *99*.
- (33) McHugh, O. L. W.; Goh, W. F.; Gradhand, M.; Stewart, D. A. Impact of impurities on the spin Hall conductivity in β -W. *Physical Review Materials* **2020**, *4*.
- (34) Vudya Sethu, K. K.; Ghosh, S.; Couet, S.; Swerts, J.; Sorée, B.; De Boeck, J.; Kar, G. S.; Garello, K. Optimization of Tungsten β -Phase Window for Spin-Orbit-Torque Magnetic Random-Access Memory. *Physical Review Applied* **2021**, *16*.
- (35) Berger, A. J.; Edwards, E. R. J.; Nembach, H. T.; Karis, O.; Weiler, M.; Silva, T. J. Determination of the spin Hall effect and the spin diffusion length of Pt from self-consistent fitting of damping enhancement and inverse spin-orbit torque measurements. *Physical Review B* **2018**, *98*.
- (36) Dolui, K.; Nikolić, B. K. Spin-memory loss due to spin-orbit coupling at ferromagnet/heavy-metal interfaces: Ab initio spin-density matrix approach. *Physical Review B* **2017**, *96*.
- (37) Han, B.; Zhang, B.; Sun, S.; Wang, B.; Guo, Y.; Cao, J. The thickness dependence of the field-like spin-orbit torque in heavy metal/CoFeB/MgO heterostructures. *Journal of Applied Physics* **2021**, *130*.
- (38) Garello, K.; Avci, C. O.; Miron, I. M.; Baumgartner, M.; Ghosh, A.; Auffret, S.;

- Boulle, O.; Gaudin, G.; Gambardella, P. Ultrafast magnetization switching by spin-orbit torques. *Applied Physics Letters* **2014**, *105*.
- (39) Swerts, J. et al. Solving the BEOL compatibility challenge of top-pinned magnetic tunnel junction stacks. 2017 IEEE International Electron Devices Meeting (IEDM). 2017; pp 38.6.1–38.6.4.
- (40) Li, K.-S.; Shieh, J.-M.; Chen, Y.-J.; Hsu, C.-L.; Shen, C.-H.; Hou, T.-H.; Lin, C.-P.; Lai, C.-H.; Tang, D. D.; Yuan-Chen Sun, J. First BEOL-compatible, 10 ns-fast, and Durable 55 nm Top-pSOT-MRAM with High TMR ($> 130\%$). 2023 International Electron Devices Meeting (IEDM). 2023; pp 1–4.
- (41) Huang, Y.; Zhang, K.; Xiao, C.; Yang, Q.; Xu, S.; Cai, W.; Zhu, D.; Yang, J.; Zhao, W. Top Spin-Orbit-Torque Switching of Magnetic Tunnel Junction With In-Situ Efficiency Quantification. *IEEE Electron Device Letters* **2025**, *46*, 1409–1412.
- (42) Gao, W.; Liao, L.; Isshiki, H.; Budai, N.; Kim, J.; Lee, H.-W.; Lee, K.-J.; Go, D.; Mokrousov, Y.; Miwa, S.; Otani, Y. Nonlocal electrical detection of reciprocal orbital Edelstein effect. *Nature Communications* **2025**, *16*.
- (43) Valenzuela, S. O.; Tinkham, M. Direct electronic measurement of the spin Hall effect. *Nature* **2006**, *442*, 176–179.
- (44) Yang, T.; Kimura, T.; Otani, Y. Giant spin-accumulation signal and pure spin-current-induced reversible magnetization switching. **2008**, *4*, 851–854, Number: 11 Publisher: Nature Publishing Group.
- (45) Sun, J. Z.; Gaidis, M. C.; O’Sullivan, E. J.; Joseph, E. A.; Hu, G.; Abraham, D. W.; Nowak, J. J.; Trouilloud, P. L.; Lu, Y.; Brown, S. L.; Worledge, D. C.; Gallagher, W. J. A three-terminal spin-torque-driven magnetic switch. *Applied Physics Letters* **2009**, *95*.

- (46) Viala, B.; Garello, K. Orbital hall effect magnetic device and method for manufacturing such a device. US Patent US20250338505A1, 2025.
- (47) Berger, H. Models for contacts to planar devices. *Solid-State Electronics* **1972**, *15*, 145–158.